Meandering particle bunches and a link between averages of time series of particle counts and higher-order moments

M. Baquero-Ruiz, F. Manke, I. Furno, A. Fasoli, and P. Ricci

École Polytechnique Fédérale de Lausanne (EPFL), Swiss Plasma Center (SPC), CH-1015 Lausanne, Switzerland

Time-averaged spatially resolved measurements are used in many fields of physics to determine spatial distributions of a physical quantity. Although one could think that time averaging suppresses all information on time variation, there are some situations in which a link can be established between time averaging and time variability. In this paper, we consider a simple system composed of a particle bunch that moves in space without deforming, and a detector placed at a point in space. The detector continuously counts the number of particles in its neighborhood. Upon sampling, the detector signal gives rise to a time series with, in general, nonvanishing variance. Time series obtained by placing the detector at different locations can then be used to obtain a time-average distribution of the number of particles by computing the time average of all the time series. We show that there is a close relationship between this average profile and higher-order statistics of the time series, including the variance and skewness. We also show a simple procedure by which individual time series can be used to determine features of the shape of the particle bunch.

I. INTRODUCTION

Spatially resolved measurements of time-varying quantities are ubiquitous in all fields of physics, from astrophysics [1,2] to plasmas [3], condensed matter [4], and atomic physics [5]. These types of measurements are often carried out using time-averaging methods which can be a consequence of the detection process itself [6], or a requirement in cases when the signal of interest is weak and, consequently, the signal-to-noise ratio (SNR) is low. Then, techniques such as lock-in amplification [7] must be used to raise the SNR, effectively yielding a time-averaged result.

The ability to determine time variations is nevertheless essential in a wide range of studies and applications. For example, real-time measurements of light distortion are routinely used to correct blurring in astronomical observations from Earth-bound telescopes [8]. Measurements of wandering of a laser beam that propagates through the atmosphere can be used to determine the strength of atmospheric turbulence [9,10]. In tokamaks, the location of mm-wave power deposition depends on wave scattering by intermittent structures in the turbulent plasma [11,12]. In all these cases, time variations associated to time-changing spatial distributions reveal information that, naively, one could think would be washed away by time averaging.

In this paper, we show that this need not be the case. We develop a model to study time variations of detection signals in the particular case where the spatial distribution moves as a whole within a bounded region and without significant deformation (see Fig. 1). The idealized system is composed of a finite-sized bunch of particles and a detector placed in a particular location that counts the number of particles in its neighborhood. Due to the motion of the bunch, the detector measures a time-changing signal, which upon sampling, constitutes a time series [13] of the number of detected particles

(TSN). We call the average of the TSN the average particle count (AC). If we then place the detector in other locations, we obtain a collection of TSNs with location-varying properties, among them the AC. The AC as a function of all possible locations of the detector is referred to as average profile (AP), and is a proxy for general time-averaged spatially resolved measurements.

We show that the AP is closely related to TSN statistics of higher order at each possible detector location. In other words, knowledge of a time-averaged spatially resolved quantity can be used to obtain local time-variability information. This is different from recent studies [14,15], where a theoretical framework is developed to obtain APs from more general models of individual bunches (including time decay) but *no* general relationship of the AP to higher-order TSN statistics is established. It is also different from the model developed by Taylor in his studies of turbulence in a streaming fluid [16], where it is shown that the frequency spectrum of fluctuation measurements at a fixed point in space can be related to the correlation of measurements performed simultaneously at two different locations joined by a streamline. Key to this result is the assumption that there are turbulent structures that are *frozen* into the flow [17] so that they move at the fixed stream velocity. In our model, we have a single particle bunch whose motion cannot be characterized by a constant velocity.

Conversely, we show that spatial information can be obtained from local time-variability information. Indeed, under certain conditions, features of the shape of the particle bunch can be obtained from the moments of individual TSNs.

Our study starts in one dimension (1D). We develop a model for the simple 1D idealized system (Sec. II A) and use it to obtain some important relations as well as expressions for the statistics of TSNs, such as the variance and skewness. We then apply the theory to a particular case that yields exact
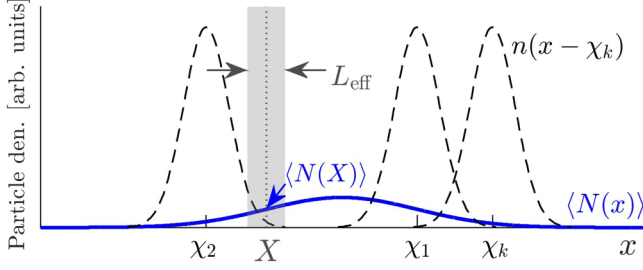
FIG. 1. One-dimensional case. A rigid particle bunch, of density $n(x)$, moves along x such that at time t_k its center is at $x = \chi_k$ (dashed lines). A detector located at $x = X$ counts the number of particles within a small region of effective length L_{eff} (gray shade), leading to a TSN with K samples. The mean of the TSN, $\langle N(X) \rangle$, converges to the AC at X for sufficiently large K.

solutions and use them to compare predictions with results from numerically generated time series. In Sec. III A, we find a way to compute TSN statistics only from knowledge of a few global parameters and more general APs. We establish conditions of validity for these results and study the effect of relaxing some of the hypotheses. We then study how the results change for different bunch shapes and, conversely, explore a procedure that allows determining shape features from single-TSN statistics.

In Sec. IV, we extend the formalism to 2D. We demonstrate the applicability of the theory to a realistic situation using as an example the propagation of fast ions in a turbulent plasma in the TORPEX [18–20] device (Sec. V). After discussing the results, we conclude with a summary and an outlook on possible future studies (Sec. VI).

Although we deal with particle counts and particle density profiles, the formalism developed in the paper can be straight-forwardly used to model any system where a quantity is measured and we expect a *rigid* motion of the corresponding spatial density profile. The results may therefore find use in different fields of physics and engineering.

II. 1D MODEL

A. Description of model

Figure 1 shows a description of our 1D model. A bunch of $N \gg 1$ particles with density profile $n(x)$ moves rigidly along x. Without loss of generality, we assume that $\int x \, n(x) \, dx = 0$ [this integral, as well as all other integrals in this work, are understood to be performed over all space, i.e., the interval $(-\infty, \infty)$]. The evolution of the system is observed at K instants $t_1 < t_2 < \cdots < t_k < \cdots < t_K$ and, for the kth sample, the center of the bunch is located at $x = \chi_k$. The overall particle density distribution at time t_k is then $n(x - \chi_k)$ and $\int n(x - \chi_k) \, dx = N$ for all k.

A detector is placed at a location $x = X$ to *instantaneously* count the number of particles near it. The probability that a particle at x will be counted, given that the detector is at X, is given by the response efficiency $L(x, X)$, which is assumed to be a function only of location relative to X. Then $L(x, X) = L(x - X)$, and $0 \leqslant L(x - X) \leqslant 1$, with zero equivalent to no response and 1 to full efficiency. We assume that $\int L(x) \, dx \equiv L_{\text{eff}}$ is finite. The number of particles counted by the detector

in sample k (time t_k) is then

$$
\begin{aligned}
N_k(X) &= \int n(x - \chi_k) \, L(x - X) \, dx \\
&= \int n(X + u - \chi_k) \, L(u) \, du,
\end{aligned} \tag{1}
$$

where u is just a dummy integration variable. The collection $\{N_k(X)\} \equiv \{N_1(X), N_2(X), \ldots, N_K(X)\}$ of all K samples of $N_k(X)$ is a TSN at detector location X.

From Eq. (1) one can see that $\int N_k(x) \, dx = L_{\text{eff}} N$ for all k. We define the normalized detected bunch profile $n_L(x)$ as

$$
n_L(x) \equiv \frac{1}{L_{\text{eff}} N} \int n(x + u) \, L(u) \, du, \tag{2}
$$

such that $\int n_L(x) \, dx = 1$ and $N_k(X) = N L_{\text{eff}} n_L(X - \chi_k)$, and use this definition to find the average number of particles detected at X, $\langle N(X) \rangle$. This is accomplished by computing the mean of all samples of $\{N_k(X)\}$:

$$
\begin{aligned}
\langle N(X) \rangle &\equiv \frac{1}{K} \sum_{k=1}^{K} N_k(X) \\
&= \frac{L_{\text{eff}} N}{K} \sum_{k=1}^{K} n_L(X - \chi_k).
\end{aligned} \tag{3}
$$

When regarded as a function of all x, $\langle N(x) \rangle$ is the AP in 1D.

In Eq. (3) one can consider $\{\chi_k\}$ as a collection of K instances of a random variable χ that follows some probability density function (PDF) $f(x)$. Given that [21–23]

$$
\frac{1}{K} \sum_{k=1}^{K} n_L(X - \chi_k) \stackrel{K \to \infty}{=} E[n_L(X - \chi)],
$$

where $E[\chi]$ is the expected value of χ and, therefore [24], $E[n_L(X - \chi)] = \int n_L(X - x) f(x) \, dx$, we obtain

$$
\langle N(X) \rangle \stackrel{K \to \infty}{=} L_{\text{eff}} N \int n_L(X - x) f(x) \, dx. \tag{4}
$$

The PDF $f(x)$ can then be understood as the number of times that the center of the bunch visits the interval $(x, x + dx)$, compared to all other locations, when sufficiently many observations are considered. As such, $f(x)$ *encapsulates* the information of the motion of the bunch.

We now define the function

$$
m(X) \equiv \frac{\langle N(X) \rangle}{L_{\text{eff}} N}, \tag{5}
$$

noticing that $m(X) \geqslant 0$ for all detector locations X and that $\int m(x) \, dx = 1$. Then, in the limit of very large K, Eq. (4) can be written as

$$
m(X) = \int n_L(X - x) f(x) \, dx. \tag{6}
$$

Equation (6) is an interesting relation, as it links a *temporal* average of the local quantity $m(X)$ to a *spatial* average of $n_L(x)$ [through $f(x)$]. It will be shown, in Secs. II B and III A, that Eq. (6) provides a way to determine f from knowledge of n_L and the AP.

One can find expressions for other moments of the TSN in a similar way. For any real $q \geqslant 1$,

$$\langle N^q(X) \rangle = \frac{1}{K} \sum_{k=1}^{K} [N_k(X)]^q$$

$$\overset{K \to \infty}{=} (L_{\text{eff}} N)^q \int [n_L(X - x)]^q f(x) \, dx.$$

The PDF $f(x)$ is the same as in Eq. (6), as it is related to the same random variable χ. Then, defining

$$m_q(X) \equiv \frac{\langle N^q(X) \rangle}{(L_{\text{eff}} N)^q}, \tag{7}$$

we have

$$m_q(X) = \int [n_L(X - x)]^q f(x) \, dx. \tag{8}$$

Notice that $m_1(x) \equiv m(x)$. Notice also that the integral of $m_q(x)$ can in general be different from 1 for $q > 1$. The choice $q = 2$ allows one to find an expression for the variance of $\{N_k(X)\}$ which, for large K, needs no bias correction [21]:

$$\text{Var}[\{N_k(X)\}] = \langle N^2(X) \rangle - \langle N(X) \rangle^2$$

$$= (L_{\text{eff}} N)^2 (m_2(X) - (m(X))^2). \tag{9}$$

The cases $q = 3$ and $q = 2$ allow us to obtain an expression for the skewness [25] S of $\{N_k(X)\}$, again assuming large K:

$$\text{S}[\{N_k(X)\}] = \frac{m_3(X) - 3 \, m(X) \, m_2(X) + 2(m(X))^3}{(m_2(X) - (m(X))^2)^{3/2}}. \tag{10}$$

A similar procedure can be followed to find expressions relating other statistics of the TSN to the functions m_q in the limit of large K. As shown in Sec. III A, it is sometimes possible to find approximations of the m_q and compute the right-hand side (RHS) of Eqs. (4), (9), and (10) using known parameters to find predictions of the TSN statistics on the left-hand side (LHS). Under certain conditions, it is even possible to find the m_q in closed form. The latter case is explored in Sec. II B.

We can also find the covariance [21,24] of TSNs obtained *simultaneously* using two identical detectors at locations X_1 and X_2:

$$\text{Cov}[\{N_k(X_1)\}, \{N_k(X_2)\}]$$

$$= \frac{1}{K} \sum_{k=1}^{K} (N_k(X_1) - \langle N(X_1) \rangle)(N_k(X_2) - \langle N(X_2) \rangle)$$

$$= \frac{(L_{\text{eff}} N)^2}{K} \left(\sum_{k=1}^{K} n_L(X_1 - \chi_k) \, n_L(X_2 - \chi_k) \right)$$

$$- \langle N(X_1) \rangle \langle N(X_2) \rangle.$$

We then get, for large K,

$$\frac{\text{Cov}[\{N_k(X_1)\}, \{N_k(X_2)\}]}{(L_{\text{eff}} N)^2}$$

$$= \int n_L(X_1 - x) \, n_L(X_2 - x) \, f(x) \, dx - m(X_1) \, m(X_2). \tag{11}$$

B. Results using Gaussian profiles

The formalism developed in Sec. II A can be applied to a situation in which exact analytical solutions can be obtained. We consider a particle bunch with a Gaussian-shaped density profile of width w_n:

$$n(x) = \frac{N}{\sqrt{2\pi \, w_n^2}} e^{-\frac{x^2}{2 w_n^2}}.$$

Then $\int x \, n(x) \, dx = 0$ and $\int n(x) \, dx = N$ as required in Sec. II A. Next, we assume that the detector has a Gaussian-shaped response of width w_L and peak efficiency (equal to 1) at $x = 0$:

$$L(x) = e^{-\frac{x^2}{2 w_L^2}}.$$

We choose $w_L = L_{\text{eff}}/\sqrt{2\pi}$ so that $\int L(x) \, dx = L_{\text{eff}}$.

Defining the following notation for the Gaussian (normalized) function,

$$\text{G}(x; \, c, \, w^2) \equiv \frac{1}{\sqrt{2\pi \, w^2}} e^{-\frac{(x-c)^2}{2 w^2}}, \tag{12}$$

we can write $n(x)/N = \text{G}(x; 0, w_n^2)$ and $L(x)/L_{\text{eff}} = \text{G}(x; 0, w_L^2)$. Replacing these expressions in Eq. (2) we obtain a Gaussian $n_L(x)$:

$$n_L(x) = \int \text{G}(x + u; 0, w_n^2) \, \text{G}(u; 0, w_L^2) \, du$$

$$= \text{G}(x; 0, w_n^2 + w_L^2).$$

The width of $n_L(x)$ is $w_{nL} = \sqrt{w_n^2 + w_L^2} = \sqrt{w_n^2 + L_{\text{eff}}^2/(2\pi)}$. As one would expect, the detector *widens* the observed bunch profile. At this point, it is worthwhile stressing that n_L is *not* a PDF as it is not associated with any random variable on its own. It is rather just a Gaussian-shaped function.

We assume now that the AP [i.e., $\langle N(x) \rangle$ in *all* x] has been determined, possibly from experiments, to also be Gaussian shaped with width w_m and mean location c_m. From Eq. (5),

$$\langle N(X) \rangle = L_{\text{eff}} N \, m(X), \tag{13}$$

so $m(X) = \text{G}(X; c_m, w_m^2)$. According to Eq. (6) we must then have

$$\text{G}(X; c_m, w_m^2) = \int \text{G}(X - x; 0, w_{nL}^2) \, f(x) \, dx.$$

This equation is satisfied with $f(x) = \text{G}(x; c_m, w_m^2 - w_{nL}^2)$. Since $f(x)$ is a PDF, this result shows that the χ_k are instances of a *Normal* random variable with mean $\mu_f = c_m$ and standard deviation $\sigma_f = \sqrt{w_m^2 - w_{nL}^2}$, which is well defined since the width of the average profile cannot be smaller than the width of the bunch profile. This procedure exemplifies how, as discussed in Sec. II A, knowledge of n_L and the AP can be used to determine f.

The preceding result is, in fact, very convenient as we can now replace n_L and f in Eq. (8) and, after some algebra (see
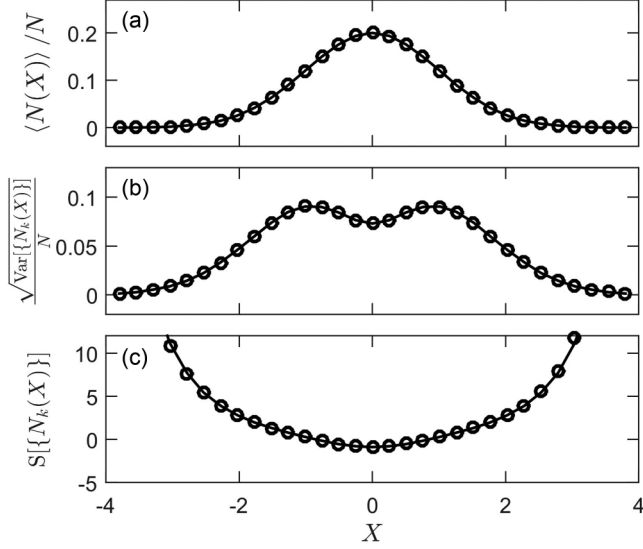
FIG. 2. Comparison of simulated values of TSN statistics (circles) to predictions (lines) of the mean (a), standard deviation (b), and skewness (c) at different detector locations X. We use $c_m = 0$, $w_m = 1$ [apparent from the width of the Gaussian profile in (a)], $w_n = 0.7$, and $w_L = 0.2$. Notice the large range of values of the skewness, which includes negative numbers close to $X = 0$.

Appendix), express the m_q in terms of m as

$$m_q(X) = \sqrt{\frac{s_q \left(2\pi\, w_m^2\right)^{s_q - 1}}{q \left(2\pi\, w_{nL}^2\right)^{q-1}}} \left(m(X)\right)^{s_q}, \quad (14)$$

where we have defined

$$s_q \equiv \left(1 - \frac{w_{nL}^2}{w_m^2}\left(1 - \frac{1}{q}\right)\right)^{-1}. \quad (15)$$

From Eqs. (9) and (14), the TSN variance satisfies

$$\frac{\mathrm{Var}[\{N_k(X)\}]}{(L_{\mathrm{eff}}\,N)^2} = \sqrt{\frac{s_2 \left(2\pi\, w_m^2\right)^{s_2 - 1}}{4\pi\, w_{nL}^2}\left(m(X)\right)^{s_2} - \left(m(X)\right)^2}. \quad (16)$$

From Eq. (10), an analytic expression for the skewness can be obtained in a similar way.

For given parameters N, w_m, w_n, and w_L, we can predict the values of the time-series statistics on the LHS of Eqs. (13) and (16) from the expressions on the RHS. Figure 2 shows an example of predictions compared to numerical results obtained with a simulation in MATLAB [26]. This simple code generates time series $\{N_k(X)\}$ with 10^5 samples using Eq. (3), the definitions of $n(x)$, $L(x)$, and $\langle N(X)\rangle$ in this section, and random numbers χ_k distributed $f(x)$. It then computes the mean, standard deviation, and skewness of $\{N_k(X)\}$ for different detector locations X. Figure 3 shows a comparison of predictions and numerical results for a wide range of detected bunch widths w_{nL}. The good agreement in all cases shows that the formalism developed in Sec. II A can accurately describe statistical features of the TSNs.

Equation (11) and the Gaussian-shaped $n(x)$, $L(x)$, and $m(X)$ also allow us to find an analytic expression for the
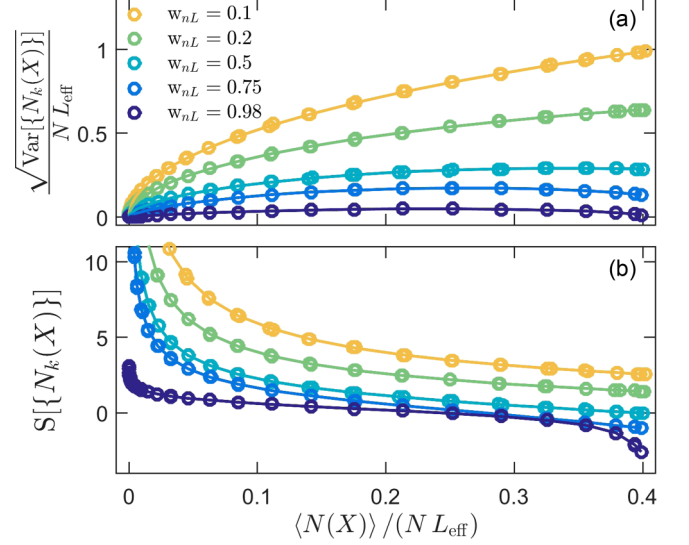

FIG. 3. Using $w_m = 1$, we compute the variance and the skewness of numerically generated TSNs $\{N_k(X)\}$ for different values of w_{nL}. (a) Simulated standard deviation plotted against the simulated mean (circles). Both the standard deviation and the mean have been normalized by $L_{\mathrm{eff}} N$. This makes it simple to compare the results against predictions (lines) and highlights the fact that TSN moments can be determined at a particular detector location X from knowledge of $\langle N(X)\rangle$ and $L_{\mathrm{eff}} N$. (b) Skewness versus normalized mean. No normalization is performed for the skewness as its value is not affected by rescalings of the $N_k(X)$.

covariance with two identical detectors at locations X_1 and X_2:

$$\frac{\mathrm{Cov}[\{N_k(X_1)\},\,\{N_k(X_2)\}]}{(L_{\mathrm{eff}}\,N)^2} = -m(X_1)\,m(X_2)$$
$$+ \sqrt{\frac{s_2 \left(2\pi\, w_m^2\right)^{s_2 - 1}}{4\pi\, w_{nL}^2}}\left[m\left(\frac{X_1 + X_2}{2}\right)\right]^{s_2} e^{-\frac{(X_1 - X_2)^2}{4 w_{nL}^2}}. \quad (17)$$

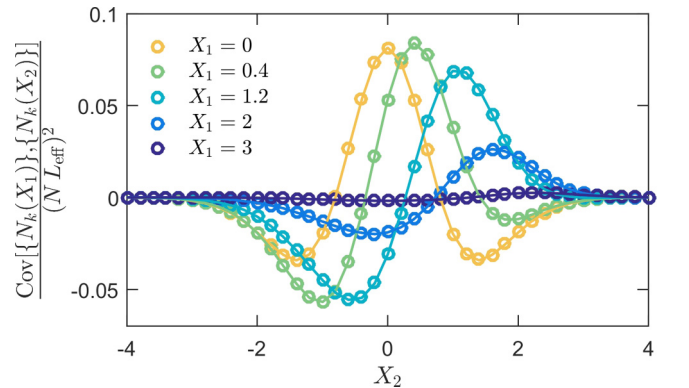FIG. 4. Numerically generated covariance (circles) of the time series at two locations X_1 and X_2. The different colors correspond to different values of X_1 as shown in the legend. We use here $c_m = 0$, $w_m = 1$, and $w_{nL} = 0.5$. The predicted covariances (lines) precisely follow the numerical results.

Figure 4 shows results of numerical simulations of the covariance that corroborate the predictions obtained with the model.

C. Effect of independent (uncorrelated) noise

Real detector systems are subject to *noise* [6,27]. Assuming noise to be additive and independent (in the statistical sense) of the actual signal, we model the noisy particle-number samples as being affected by independent instances $\eta_k(X)$ of the random variable $\eta(X)$, with mean $\mu_\eta(X)$, variance $\sigma_\eta^2(X)$, and skewness $\gamma_\eta(X)$:

$$\mathcal{N}_k(X) \equiv N_k(X) + \eta_k(X). \tag{18}$$

Notice that we allow for noise to change with the detector location X. The *noisy* detected time series is $\{\mathcal{N}_k(X)\}$. Then

$$\langle \mathcal{N}(X) \rangle = \langle N(X) \rangle + \mu_\eta(X)$$
$$= (L_{\text{eff}} N) m(X) + \mu_\eta(X). \tag{19}$$

Statistical independence of the noise allows one to drop terms in summations that involve products of the $N_k(X)$ and $\eta_k(X)$, leading to the following expressions for the variance,

$$\text{Var}[\{\mathcal{N}_k(X)\}] = \text{Var}[\{N_k(X)\}] + \sigma_\eta^2(X)$$
$$= (L_{\text{eff}} N)^2 (m_2(X) - (m(X))^2) + \sigma_\eta^2(X), \tag{20}$$

and the skewness,

$$\text{S}[\{\mathcal{N}_k(X)\}](\text{Var}[\{\mathcal{N}_k(X)\}])^{3/2}$$
$$= \frac{1}{K} \sum_{k=1}^{K} ((N_k(X) - \langle N(X) \rangle) + (\eta_k(X) - \mu_\eta(X)))^3$$
$$= \text{S}[\{N_k(X)\}](\text{Var}[\{N_k(X)\}])^{3/2} + \gamma_\eta(X) \sigma_\eta^3(X).$$

Equation (10) allows us to write the skewness in terms of the m_q:

$$\text{S}[\{\mathcal{N}_k(X)\}]$$
$$= \frac{m_3(X) - 3 m(X) m_2(X) + 2(m(X))^3 + \frac{\gamma_\eta(X)\sigma_\eta^3(X)}{(L_{\text{eff}} N)^3}}{\left(m_2(X) - (m(X))^2 + \frac{\sigma_\eta^2(X)}{(L_{\text{eff}} N)^2}\right)^{3/2}}.$$
$$\tag{21}$$

This last expression shows that noise can greatly affect the value of skewness. Indeed, if $\sigma_\eta^2(X) \gg \text{Var}[\{N_k(X)\}]$, then $\text{S}[\{\mathcal{N}_k(X)\}] \to \gamma_\eta(X)$, so the true skewness can be completely obscured. An example of the effect of varying levels of noise on the value of the variance and skewness is shown in Fig. 5.

The covariance of the noisy TSN at X_1 and X_2 is

$$\text{Cov}[\{\mathcal{N}_k(X_1)\}, \{\mathcal{N}_k(X_2)\}]$$
$$= \text{Cov}[\{N_k(X_1)\}, \{N_k(X_2)\}] + \text{Cov}[\{\eta_k(X_1)\}, \{\eta_k(X_2)\}], \tag{22}$$

where we have further assumed that noise is independent of the signal *irrespective* of location. As one would expect,
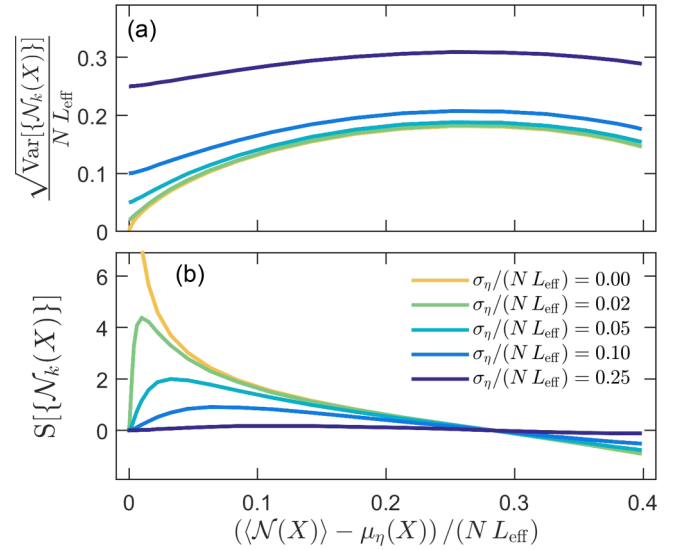

FIG. 5. Normalized standard deviation (a) and skewness (b) of the noisy TSN $\{\mathcal{N}_k(X)\}$, plotted against the normalized mean, for varying levels of noise (as indicated in the legend). We assume Gaussian-shaped $n(x)$, $L(x)$, and $\langle N(x) \rangle$, as in Fig. 2, with parameters $c_m = 0$, $w_m = 1$, $w_n = 0.7$, and $w_L = 0.2$, and Gaussian noise with μ_η, σ_η independent of the detector location X (clearly $\gamma_\eta = 0$). These predictions are obtained from Eqs. (19), (20), and (21). Notice that even small values of noise force the skewness to fall to zero in regions of weak signal, i.e., where $\langle \mathcal{N}(X) \rangle - \mu_\eta(X) = 0$.

the covariance is affected by noise that exhibits a correlation between locations X_1 and X_2.

III. APPROXIMATIONS FOR MORE GENERAL 1D AVERAGE PARTICLE COUNT PROFILES

A. Approximations

In Sec. II B we solved Eq. (6) for Gaussian m and n_L. We found a solution f of similar shape (a *Normal* PDF) and width $\sigma_f^2 = w_m^2 - w_{nL}^2 = w_m^2(1 - w_{nL}^2/w_m^2)$. If $w_{nL} < w_m$, this suggests that the functional forms of f and m may differ only by small corrections in w_{nL}/w_m. We now show that this is indeed the case, even when m has a non-Gaussian (but anyway integrable) profile.

For simplicity, we still assume $n_L(x) = \text{G}(x; 0, w_{nL}^2)$, although other shapes can be explored in a similar way (see Sec. III B). We perform an expansion of $f(x)$ around the detector location X such that $f(x) \approx f(X) + f'(X)(x - X) + (1/2) f''(X)(x - X)^2 + O[(x - X)^3]$ and, up until third order (due to symmetry of n_L),

$$m(X) = \int n_L(X - x) f(x) dx \approx f(X) + \frac{w_{nL}^2}{2} f''(X)$$
$$\approx f(X) \quad (\text{if } w_{nL}^2 |f''(X)| \ll f(X)). \tag{23}$$

In this expression, one can think of $|f''(x)| \sim f(x)/L_{\text{typ}}^2$, where L_{typ} is some typical variation length of $f(x)$. Then $f(x) \approx m(x)$ if $w_{nL}^2/L_{\text{typ}}^2 \ll 1$, in a way similar to the discussion of a Gaussian m above.
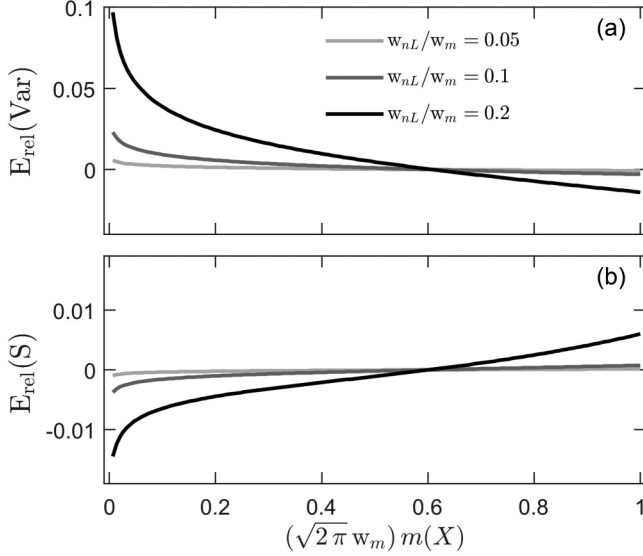
FIG. 6. (a) Relative error between the predicted variance [RHS in Eq. (9)] using approximations [i.e., using Eq. (25)] and using exact expressions of m_q [Eq. (14)], for the case with no noise and Gaussian $m(X)$. The error is computed as $E_{rel}(Var) = [Var_{appr}(X) - Var_{exact}(X)]/Var_{exact}(X)$ and analogously for the skewness. (b) Relative error between predicted skewness using approximations and using exact expressions. Notice that these results are valid for any $w_m > 0$. Indeed, the expressions for the errors can be cast in a form that only depends on w_{nL}/w_m and $\sqrt{2\pi}\, w_m\, m(X)$.

The functions m_q can be computed in a similar way:

$$
\begin{aligned}
m_q(X) &\approx f(X) \int [n_L(x)]^q dx + \frac{f''(X)}{2} \int x^2 [n_L(x)]^q dx \\
&\approx f(X) \int [n_L(x)]^q dx \quad (\text{if } w_{nL}^2 |f''(X)| \ll f(X)),
\end{aligned}
$$
(24)

where the last line follows from $\int x^2 [n_L(x)]^q dx = (w_{nL}^2/q) \int [n_L(x)]^q dx$ for the Gaussian $n_L(x)$ with zero mean and $q \geqslant 1$. Then, combining this result with Eq. (23), we obtain

$$
\begin{aligned}
m_q(X) &\approx m(X) \int [n_L(x)]^q dx \\
&= \frac{1}{\sqrt{q}} \left(n_L^{max} \right)^{q-1} m(X)
\end{aligned}
$$
(25)

valid for $w_{nL}^2 |m''(X)| \ll m(X)$ and $q \geqslant 1$. In this expression n_L^{max} is the maximum of $n_L(x)$, i.e., $n_L^{max} = n_L(0) = 1/\sqrt{2\pi w_{nL}^2}$.

The $m_q(X)$ obtained in Eq. (25) can be replaced in Eqs. (9) and (10) [or, in the noisy case, Eqs. (20) and (21)] to find approximate values of variance and skewness of TSNs in the case of small w_{nL}/w_m considered here. Figure 6 shows a comparison between predictions that use the exact expressions for Gaussian $m(X)$ in Secs. II B and II C, with predictions using the approximations. The agreement is good to within 10% in variance and 2% in skewness in all X for $w_{nL}/w_m \leqslant 0.2$. Since these two statistics depend only on the value of $m(X)$
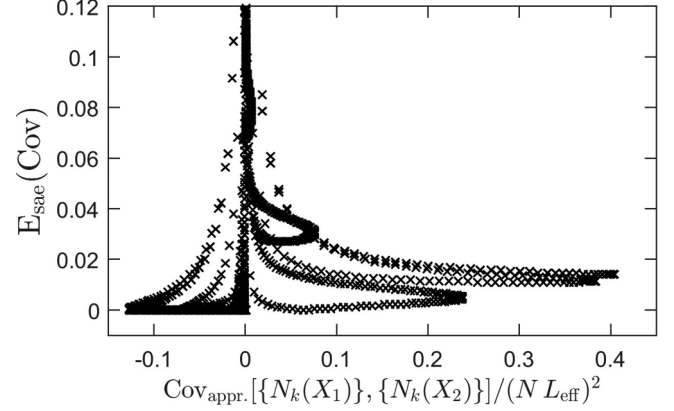

FIG. 7. Error in the covariance when using the approximation [Eq. (26)] compared to the exact result [Eq. (17)] for Gaussian-shaped m ($c_m = 0$, $w_m = 1$) and n_L ($w_{nL} = 0.2$). Each marker represents one choice of X_1, X_2, where $X_1 = 0, 0.4, 1.2, 2$, or 3 and $X_2 \in [-5, 5]$. To better compare values near *zero* crossings, we use the symmetric absolute error $E_{sae}(Cov) = 2|Cov_{appr} - Cov_{exact}|/(|Cov_{appr}| + |Cov_{exact}|)$ instead of the more common relative error. An $E_{sae} \leqslant 0.1 = 10\%$ is observed for all values of the approximate covariance Cov_{appr} except very close to *zero*, where small denominators make the error estimation impractical.

and not explicitly on X [exemplified by the fact that Fig. 6 is plotted against $m(X)$], we expect other more general $m(X)$ profiles to show a similar behavior. Simulations may however be required in non-Gaussian cases where higher accuracy is desired.

Under the same conditions as in Eq. (25), the covariance can be approximated by

$$
\begin{aligned}
\frac{Cov[\{N_k(X_1)\}, \{N_k(X_2)\}]}{(L_{eff}\, N)^2} &\approx -m(X_1)\, m(X_2) \\
&\quad + m\left(\frac{X_1 + X_2}{2} \right) G(X_1 - X_2; 0, 2 w_{nL}^2).
\end{aligned}
$$
(26)

Figure 7 shows expected errors in the covariance by comparing results from Eq. (26) and Eq. (17) in the case $w_m = 1$, $w_{nL} = 0.2$. The agreement is good to within 10% except near *zero* covariance, where the computation of the error is problematic due to small denominators. The agreement becomes better for smaller values of w_{nL}, as in the case of the variance and skewness above.

B. Other bunch shapes

Equation (24) is valid for arbitrary n_L and $q \geqslant 1$, provided $\int x[n_L(x)]^q dx = 0$ and $\int x^2 [n_L(x)]^q dx \leqslant w_{nL}^2 \int [n_L(x)]^q dx$, where in this more general case $w_{nL}^2 \equiv \int x^2 n_L(x)\, dx$. Figure 8(a) shows some examples of n_L that fulfill these requirements.

If $w_{nL}^2 |m''(X)| \ll m(X)$, we then similarly have $m_q(X) \approx m(X) \int [n_L(x)]^q dx$. In this case, however, the value of the integral $\int [n_L(x)]^q dx$ will change for different choices of n_L. A direct computation shows that

$$
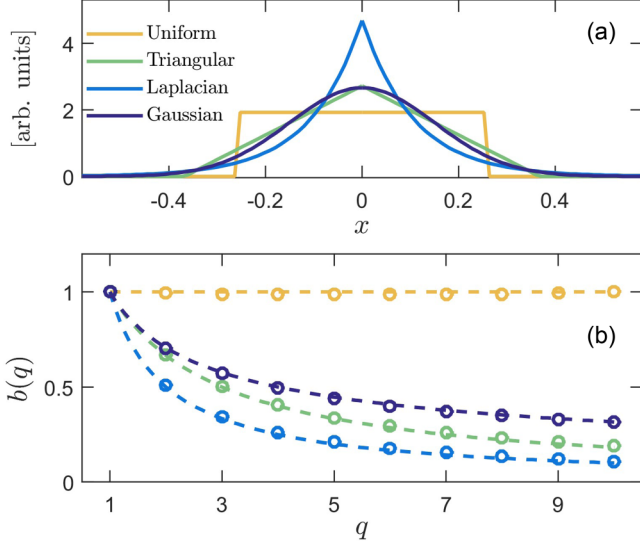\int [n_L(x)]^q dx = \left(n_L^{max} \right)^{q-1} b(q),
$$
(27)

FIG. 8. (a) Some possible shapes for n_L that fulfill the requirements for the approximations in Sec. III A. All shapes are correctly normalized to integrate to 1 and have $w_{n_L} = 0.15$. (b) Application of Eq. (31) to numerically generated TSNs using the $n_L(x)$ shown in (a), $f(x) = G(x; 0, 1 - w_{n_L}^2)$, and $K = 10^5$ gives the results shown with circles [same color labeling as in (a)]. The detector location is $X = 0$ in all cases. Gaussian noise is added with $\mu_\eta = 0$ and $\sigma_\eta = 0.2 \times N^{\max}$, and $N^{\max}$ is determined from the known parameters (it is *not* estimated from the TSNs). The agreement with the expressions for $b(q)$ in Eq. (28) (dashed lines) allows one to distinguish shapes based on information gathered from a single TSN.

where, remembering that $q \geqslant 1$,

$$b(q) = \begin{cases} 1 & \text{if } n_L \text{ is uniform,} \\ \frac{1}{\sqrt{q}} & \text{if } n_L \text{ is Gaussian,} \\ \frac{2}{q+1} & \text{if } n_L \text{ is triangular,} \\ \frac{1}{q} & \text{if } n_L \text{ is Laplacian [23].} \end{cases} \tag{28}$$

The different shapes considered here are depicted in Fig. 8(a).

Equations (27) and (28) can be regarded as a link between bunch shapes and the function $b(q)$. They are useful whenever one wants to find approximate expressions for the variance and skewness of TSNs in the case when the bunch is not Gaussian shaped [see Eqs. (9), (10), (20), and (21)]. This link also provides a way to explore the inverse problem, i.e., the determination of features of bunches from TSNs.

Using the definitions of $m(X)$ and the $m_q(X)$ in Eqs. (5) and (7), together with Eq. (27), we can rewrite the relation $m_q(X) \approx m(X) \int [n_L(x)]^q dx$ as

$$\frac{\langle N^q(X) \rangle}{(L_{\text{eff}} N)^q} \approx \frac{\langle N(X) \rangle}{L_{\text{eff}} N} \left(n_L^{\max} \right)^{q-1} b(q). \tag{29}$$

Upon noticing [see discussion after Eq. (2)] that $N^{\max} \equiv L_{\text{eff}} N n_L^{\max} = \max[\{N_k(X)\}]$, the maximum value of the time series detected at X, Eq. (29) leads to

$$b(q) \approx \frac{\langle N^q(X) \rangle}{(N^{\max})^{q-1} \langle N(X) \rangle}. \tag{30}$$

Here, of course, we assume that K is sufficiently large for statistical (sample-size related) errors to be negligible.

From *only* knowledge of the TSN at the single detector location X, Eq. (30) provides a way to determine $b(q)$ for all $q \geqslant 1$. Since $b(q)$ only depends on integrals of n_L [recall Eq. (27)], comparison of an experimental $b(q)$ with plots of Eq. (28) gives an idea of the compatibility of the experimental bunch shape with any one of the four theoretical cases considered for n_L.

In practice, though, there are two problems with the application of Eq. (30). The first one is noise. As seen in Sec. II C, noise may greatly affect the values of TSN statistics and must therefore be taken into account. The second problem is the estimation of $N^{\max}$. This can be a difficult task, especially in detector locations with low $\langle N(X) \rangle$ as, then, it is expected that the bunch visits be infrequent and few instances of the maximum (if any at all) be observed in a finite amount of time.

Assuming anyway that $N^{\max}$ can be determined with negligible error even in the presence of noise, we now consider the case of the noisy TSN $\{\mathcal{N}_k(X)\}$ as in Eq. (18). We notice that some TSN samples $\mathcal{N}_k(X)$ may be negative due to noise, so we restrict the analysis to integer values of $q \geqslant 1$ to avoid complications with fractional powers. Since noise is statistically independent from the signal,

$$\langle \mathcal{N}^q(X) \rangle = \frac{1}{K} \sum_{k=1}^{K} [N_k(X) + \eta_k(X)]^q$$
$$= \sum_{j=0}^{q} \binom{q}{j} \langle N^j(X) \rangle \langle \eta^{q-j}(X) \rangle,$$

where $\langle \eta^q(X) \rangle \equiv (1/K) \sum_{k=1}^{K} [\eta_k(X)]^q$. Keeping in mind that $\langle \mathcal{N}(X) \rangle = \langle N(X) \rangle + \langle \eta(X) \rangle$, we can use this expression together with Eq. (30) to find

$$b(q) + \sum_{j=1}^{q-1} \binom{q}{j} \frac{\langle \eta^{q-j}(X) \rangle}{(N^{\max})^{q-j}} b(j)$$
$$= \frac{1}{(N^{\max})^{q-1}} \frac{\langle \mathcal{N}^q(X) \rangle - \langle \eta^q(X) \rangle}{\langle \mathcal{N}(X) \rangle - \langle \eta(X) \rangle}, \tag{31}$$

valid for $q \geqslant 2$, and $b(1) = 1$. Thus, if we are able to determine a time series $\{\eta_k(X)\}$ of only the noise, we can use Eq. (31) to solve for $b(q)$ in ascending order $q = 1, 2, \ldots, Q$ to find $b(2), b(3), \ldots, b(Q)$ up to any integer $Q \geqslant 2$.

Figure 8(b) shows results of $b(q)$ obtained using Eq. (31) from numerical simulations of noisy TSNs and different choices of n_L. The compatibility of the simulations with the curves for the different shapes is an example of the practical applicability of this procedure.

C. Bunch density profile variations

So far, it has been assumed that $n(x)$ does not change over time. We now study small variations of $n(x)$.

We assume that the density profile $n(x)$ depends on an additional parameter λ which is related to its shape but does not alter the mean. For example, if $n(x)$ is Gaussian-like, then λ could be the width. This is made explicit by renaming the particle density $n(x, \lambda)$ and having $\int n(x, \lambda) dx = N$ for all λ, i.e., the total number of particles in the bunch is the same

independent of any changes in shape. Also, we require that $\int x\, n(x, \lambda)\, dx = 0$.

We then allow λ to change over time, so that at time t_k (kth sample) it has the value λ_k. $N_k(X)$ in Eq. (1) is redefined as

$$N_k(X) = \int n(X + u - \chi_k, \lambda_k)\, L(u)\, du$$

and $N_k(X) = N\, L_{\text{eff}}\, n_L(X - \chi_k, \lambda_k)$. The mean particle number detected at X then becomes

$$\langle N(X) \rangle = \frac{L_{\text{eff}}\, N}{K} \sum_{k=1}^{K} n_L(X - \chi_k, \lambda_k)$$

$$\stackrel{K \to \infty}{=} L_{\text{eff}}\, N \iint n_L(X - x, l)\, h(x, l)\, dx\, dl$$

in a similar way as argued in the derivation of Eq. (4). This time, however, the χ_k and λ_k come from a joint PDF $h(x, l)$ which, in general, allows the motion of the bunch to be correlated with changes in shape.

For what follows, however, we assume that *motion* and *shape* are statistically independent, so $h(x, l) = f(x)\, g(l)$, where f and g are PDFs of a single variable. Then, $\iint n_L(X - x, l)\, h(x, l)\, dx\, dl = \int [\int n_L(X - x, l)\, g(l)\, dl]\, f(x)\, dx$. The function

$$\overline{n_L}(x) \equiv \int n_L(x, l)\, g(l)\, dl \tag{32}$$

can be understood as an *average* profile in terms of shape. Notice that $\int \overline{n_L}(x)\, dx = 1$ and $\int x\, \overline{n_L}(x)\, dx = 0$. With this definition, we can write

$$m(X) \equiv \frac{\langle N(X) \rangle}{L_{\text{eff}}\, N} \stackrel{K \to \infty}{=} \int \overline{n_L}(X - x)\, f(x)\, dx \tag{33}$$

in a very similar way to Eqs. (4), (5), and (6), except that in this case we use the *average* bunch profile [Eq. (32)].

In order to compute the m_q, we make first the following definition:

$$\delta n_L^j(x) \equiv \int [n_L(x, l) - \overline{n_L}(x)]^j\, g(l)\, dl.$$

We observe that, for fixed x, $\delta n_L^j(x)$ is just the jth central moment of the random quantity $n_L(x, \lambda)$, where λ is distributed $g(l)$.

For any integer $q \geqslant 1$,

$$m_q(X) = \int [\overline{n_L}(X - x)]^q\, f(x)\, dx + \Delta m_q(X), \tag{34}$$

where we have introduced

$$\Delta m_q(X) = \sum_{j=2}^{q} \binom{q}{j} \int \delta n_L^j(X - x)\, [\overline{n_L}(X - x)]^{q-j}\, f(x)\, dx.$$

Notice that the summation does not include the case $j = 1$ as, by definition, $\delta n_L^1(x) = 0$.

The Δm_q can be seen as corrections to the m_q due to additional variability from bunch shape changes. It is in general difficult to evaluate them explicitly for arbitrary $g(l)$ and, in most cases, we have to resort to simulations (see, for example, Sec. V). However, there is a particular case that can be very illuminating, specifically in the cases $q = 2, 3$ of importance in our TSN studies.

For fixed x, we assume that $n_L(x, \lambda)$ is distributed *Gamma*. This is a very general PDF for nonnegative random variables that includes other common distributions as special cases [24].

If $\delta n_L^2(x) \ll [\overline{n_L}(x)]^2$, which corresponds to *Gamma* distributions with shape parameter [24] $\alpha(x) = [\overline{n_L}(x)]^2 / \delta n_L^2(x) \gg 1$, we obtain a value of Δm_2 and Δm_3 that is small compared to the first term on the RHS of Eq. (34) for $q = 2, 3$, respectively. We have, to order $\delta n_L^2(x)/[\overline{n_L}(x)]^2$,

$$\Delta m_2(X) = \int \delta n_L^2(X - x)\, f(x)\, dx,$$
$$\Delta m_3(X) \approx 3 \int \delta n_L^2(X - x)\, \overline{n_L}(X - x)\, f(x)\, dx. \tag{35}$$

As in Sec. III A, we focus on the case of a Gaussian $\overline{n_L}$ of width $w_{\overline{nL}}$. Using Eq. (33) and similar arguments as before [see discussion leading to Eq. (23)], we have $f(X) \approx m(X)$ for $w_{\overline{nL}}^2 |m''(X)| \ll m(X)$.

For this narrow Gaussian $\overline{n_L}$, the first term on the RHS of Eq. (34) gives results similar to Eq. (25). Since $\alpha(x) > 1$ for all x,

$$\int x^2\, \delta n_L^2(x)\, dx = \int x^2\, \frac{[\overline{n_L}(x)]^2}{\alpha(x)}\, dx$$

$$< \int x^2\, [\overline{n_L}(x)]^2\, dx = w_{\overline{nL}}^2,$$

therefore narrow $\overline{n_L}$ (i.e., small $w_{\overline{nL}}$) implies narrow $\delta n_L^2(x)$, this time in terms of variation along x. This motivates performing approximations of Eq. (35) similar to those of Eq. (33). Collecting results, we get

$$m_2(X) \approx \left(\frac{\overline{n_L}^{\max}}{\sqrt{2}} + \int \delta n_L^2(x)\, dx \right) m(X),$$

$$m_3(X) \approx \left(\frac{(\overline{n_L}^{\max})^2}{\sqrt{3}} + 3 \int \delta n_L^2(x)\, \overline{n_L}(x)\, dx \right) m(X),$$

where $\overline{n_L}^{\max} = (2\pi\, w_{\overline{nL}}^2)^{-1/2}$ is the maximum of $\overline{n_L}(x)$.

These expressions may have conditions of validity that are more stringent compared to Eq. (25), as the approximations depend on the exact profile of bunch shape variances $\delta n_L^2(x)$. Nevertheless, they show that, given $\alpha(x) \gg 1$, $m_2(X)$ and $m_3(X)$ are very nearly the expressions for no shape change, provided one uses the *average* bunch profile $\overline{n_L}(x)$.

The calculation of the covariance can also be shown to involve only the average bunch profile in leading terms. However, establishing the order of magnitude of the corrections involves determining a model for correlations of deformations at different points of n_L. This will depend strongly on the particularities of the shape changes and, therefore, simulations are needed to establish their impact on the statistic.

IV. 2D MODEL AND APPROXIMATIONS

We can use the same concepts of previous sections to find a link between time-series statistics and the 2D average detected particle number.

Figure 9 illustrates the situation in 2D. Similarly as in Sec. II A, the bunch density profile n is assumed to be rigid and contain a total of $N \gg 1$ particles. However, it
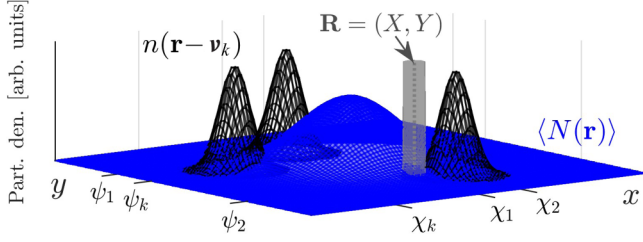
FIG. 9. Two-dimensional case. A rigid particle bunch (black) of density $n(\mathbf{r})$ moves on the xy plane such that its center at time t_k is located at $\mathbf{r} = \boldsymbol{\nu}_k = (\chi_k, \psi_k)$. A detector at $\mathbf{r} = \mathbf{R} = (X, Y)$ counts the number of particles within a region of effective area A_{eff} (shaded light gray) near $\mathbf{R}$. At large K, the detector will have recorded an AC $\langle N(\mathbf{R}) \rangle$.

now depends on two dimensions $(x, y) \equiv \mathbf{r}$, so $\int n(\mathbf{r}) \, d\mathbf{r} \equiv \int n(x, y) \, dx \, dy = N$. For simplicity, and without loss of generality, we assume again a *zero* mean, i.e., $\int \mathbf{r} \, n(\mathbf{r}) \, d\mathbf{r} = (0, 0)$.

As before, we observe the evolution of the system at K different instants. At sample time t_k, the overall particle density distribution is $n(\mathbf{r} - \boldsymbol{\nu}_k)$, where $\boldsymbol{\nu}_k \equiv (\chi_k, \psi_k)$ is the location of the bunch center. The particles are instantaneously counted by a homogeneous detector located at $\mathbf{r} = \mathbf{R} \equiv (X, Y)$, which has a 2D response efficiency $A(\mathbf{r} - \mathbf{R})$.

Defining

$$n_A(\mathbf{r}) \equiv \frac{1}{A_{\text{eff}} N} \int n(\mathbf{r} + \mathbf{u}) \, A(\mathbf{u}) \, d\mathbf{u}, \qquad (36)$$

where $\mathbf{u}$ is just a dummy integration variable and $A_{\text{eff}} \equiv \int A(\mathbf{r}) \, d\mathbf{r}$ is the *finite* effective area of the detector, we obtain an expression for the number of particles detected at location $\mathbf{R}$ and time t_k,

$$N_k(\mathbf{R}) = N A_{\text{eff}} \, n_A(\mathbf{R} - \boldsymbol{\nu}_k),$$

where n_A satisfies $\int n_A(\mathbf{r}) \, d\mathbf{r} = 1$. The ordered collection $\{N_k(\mathbf{R})\} \equiv \{N_1(\mathbf{R}), \dots, N_K(\mathbf{R})\}$ is the corresponding TSN. If

$$\langle N(\mathbf{R}) \rangle = \frac{1}{K} \sum_{k=1}^{K} N_k(\mathbf{R}),$$

we follow a similar procedure as in Eqs. (3), (4), and (6) to obtain

$$m(\mathbf{R}) \overset{K \to \infty}{=} \int n_A(\mathbf{R} - \mathbf{r}) \, f(\mathbf{r}) \, d\mathbf{r}, \qquad (37)$$

where $m(\mathbf{r}) \equiv \langle N(\mathbf{r}) \rangle / (A_{\text{eff}} N)$ is the normalized AP in 2D. The function $f(\mathbf{r})$ is the PDF of the $\boldsymbol{\nu}_k$ and, as such, encloses the information of the motion of the bunch.

The equivalent of Eq. (8) for 2D is

$$m_q(\mathbf{R}) \equiv \frac{\langle N^q(\mathbf{R}) \rangle}{(A_{\text{eff}} N)^q} = \int [n_A(\mathbf{R} - \mathbf{r})]^q \, f(\mathbf{r}) \, d\mathbf{r}, \qquad (38)$$

valid for large K and $q \geqslant 1$.

Following the same procedure of Sec. III A, we can find an approximate solution for $f(\mathbf{r})$ in Eq. (37). In 2D, the normalized Gaussian [23] function is

$$G(\mathbf{r}; \mathbf{c}, \mathbf{W}) \equiv \frac{1}{2\pi \sqrt{\det(\mathbf{W})}} e^{-\frac{1}{2}(\mathbf{r} - \mathbf{c})^T \mathbf{W}^{-1}(\mathbf{r} - \mathbf{c})}, \qquad (39)$$

where $\mathbf{W}$ is the matrix

$$\mathbf{W} = \begin{pmatrix} \mathrm{w}_x^2 & \rho \, \mathrm{w}_x \mathrm{w}_y \\ \rho \, \mathrm{w}_x \mathrm{w}_y & \mathrm{w}_y^2 \end{pmatrix}.$$

Here $-1 < \rho < 1$ can be understood as a parameter determining the orientation of the possibly elliptic shape and w_x, w_y the widths along the x and y directions. Then, for a Gaussian centered at the origin, $n_A(\mathbf{r}) = n_A(x, y) = G(\mathbf{r}; \mathbf{0}, \mathbf{W}_{nA})$, we have

$$f(\mathbf{R}) \approx m(\mathbf{R})$$

provided

$$m(\mathbf{R}) \gg \left| \rho_{nA} \, \mathrm{w}_{nA,x} \, \mathrm{w}_{nA,y} \, \frac{\partial^2 m(\mathbf{R})}{\partial x \, \partial y} \right.$$
$$\left. + \frac{1}{2} \mathrm{w}_{nA,x}^2 \frac{\partial^2 m(\mathbf{R})}{\partial x^2} + \frac{1}{2} \mathrm{w}_{nA,y}^2 \frac{\partial^2 m(\mathbf{R})}{\partial y^2} \right|. \qquad (40)$$

This is a condition on the *widths* of n_A similar to the condition obtained for Eq. (25). From similar arguments, it is approximately second order in the ratio of the widths of n_A and m. This condition is also sufficient for

$$m_q(\mathbf{R}) \approx m(\mathbf{R}) \int [n_A(\mathbf{r})]^q \, d\mathbf{r}$$
$$= \frac{1}{q} \left(n_A^{\max} \right)^{q-1} m(\mathbf{R}) \qquad (41)$$

to be valid for all $q \geqslant 1$. Here $n_A^{\max} = n_A(0, 0) = (2\pi \, \mathrm{w}_{nA,x} \, \mathrm{w}_{nA,y} \sqrt{1 - \rho_{nA}^2})^{-1}$, which has units of inverse length *squared*, different from Eq. (25). This expression also has a factor $1/q$ instead of $1/\sqrt{q}$, as in Sec. III A.

The expressions for the variance and skewness of the TSN in 2D can be obtained in a way similar to Eqs. (9) and (10). If noise is included as $\mathcal{N}_k(\mathbf{R}) \equiv N_k(\mathbf{R}) + \eta_k(\mathbf{R})$, as in Sec. II C, then Eqs. (19)–(21) together with Eq. (41) yield

$$\langle \mathcal{N}(\mathbf{R}) \rangle = A_{\text{eff}} N m(\mathbf{R}) + \mu_\eta(\mathbf{R}), \qquad (42)$$

where $\mu_\eta(\mathbf{R})$ is the noise mean at detector location $\mathbf{R}$,

$$\frac{\mathrm{Var}[\{\mathcal{N}_k(\mathbf{R})\}]}{(A_{\text{eff}} N)^2} \approx \frac{n_A^{\max}}{2} m(\mathbf{R}) - (m(\mathbf{R}))^2 + \frac{\sigma_\eta^2(\mathbf{R})}{(A_{\text{eff}} N)^2}, \qquad (43)$$

where $\sigma_\eta^2(\mathbf{R})$ is the noise variance at $\mathbf{R}$, and

$$\mathrm{S}[\{\mathcal{N}_k(\mathbf{R})\}]$$
$$\approx \frac{\frac{(n_A^{\max})^2 m(\mathbf{R})}{3} - \frac{3 n_A^{\max} (m(\mathbf{R}))^2}{2} + 2(m(\mathbf{R}))^3 + \frac{\gamma_\eta(\mathbf{R}) \sigma_\eta^3(\mathbf{R})}{(A_{\text{eff}} N)^3}}{\left(\frac{n_A^{\max}}{2} m(\mathbf{R}) - (m(\mathbf{R}))^2 + \frac{\sigma_\eta^2(\mathbf{R})}{(A_{\text{eff}} N)^2} \right)^{3/2}},$$
$$\qquad (44)$$

where $\gamma_\eta(\mathbf{R})$ is the skewness of the noise at $\mathbf{R}$.

Equations (43) and (44) have been obtained for very large K and a *narrow* Gaussian n_A which fulfills Eq. (40) and does not change shape over time. From Sec. III C, we expect these results to be reasonably robust to small shape changes, an important aspect for their usefulness in more realistic applications. Nevertheless, performing a similar analysis in 2D is cumbersome and more difficult to interpret. We therefore rely on simulations (see Sec. V) to demonstrate the predictive power of the equations.

Similarly as in Eqs. (22) and (26), the covariance can be expressed as

$$
\frac{\text{Cov}[\{\mathcal{N}_k(\mathbf{R}_1)\}, \{\mathcal{N}_k(\mathbf{R}_2)\}]}{(A_{\text{eff}} N)^2} \approx -m(\mathbf{R}_1)\, m(\mathbf{R}_2)
$$
$$
+ m\left(\frac{\mathbf{R}_1 + \mathbf{R}_2}{2}\right) G(\mathbf{R}_1 - \mathbf{R}_2;\, \mathbf{0},\, 2\,\mathbf{W}_{nA})
$$
$$
+ \frac{\text{Cov}[\{\eta_k(\mathbf{R}_1)\}, \{\eta_k(\mathbf{R}_2)\}]}{(A_{\text{eff}} N)^2} \tag{45}
$$

for very large K. Here we use Eq. (39) for the definition of the 2D Gaussian function. This expression is a good approximation whenever Eqs. (41), (43), and (44) are valid.

Given the similarity of Eq. (41) and Eq. (25), bunch shapes different than Gaussian can be treated in a way very similar to Sec. III B. Indeed, the function $b(q)$ that relates bunch shapes and TSN moments can be defined as in Eq. (27). Then, some possible 2D generalizations of the symmetric, zero-mean, shapes considered earlier yield

$$
b(q) = \begin{cases} 1 & \text{if } n_A \text{ is uniform,} \\ \frac{1}{q} & \text{if } n_A \text{ is Gaussian,} \\ \frac{6}{q^2 + 3q + 2} & \text{if } n_A \text{ is conical,} \\ \frac{1}{q^2} & \text{if } n_A \text{ is Laplacian.} \end{cases} \tag{46}
$$

To avoid confusion with other conventional definitions, the functional form of the 2D Laplacian function considered here is

$$
n_A(x, y) = \frac{3\, e^{-\sqrt{\frac{3x^2}{\text{w}_{nA,x}^2} + \frac{3y^2}{\text{w}_{nA,y}^2}}}}{2\pi\ \text{w}_{nA,x} \text{w}_{nA,y}}.
$$

Equation (46) can be used for the inverse problem as well, that is, to check the compatibility of a given TSN with an assumed bunch shape. The procedure would use an expression similar to Eq. (31) to create a plot of $b(q)$ against q. Comparison with the aforementioned theoretical values would then give an idea of the shape of n_A.

V. SIMULATIONS OF A FAST ION BEAM IN TORPEX AND COMPARISON WITH 2D MODEL

A. Description of simulations

As an example of the applicability of the formalism developed in previous sections, we analyze the results of simulations of fast ion trajectories in the TORoidal Plasma EXperiment (TORPEX) under the light of Sec. IV.

TORPEX [18] is a toroidal plasma device of major and minor radii 1 m and 20 cm, respectively, where plasmas [28] of hydrogen (or possibly other gases) are produced by absorption of 2.45 GHz microwaves at the electron-cyclotron and upper-hybrid resonances [29]. Typically, TORPEX plasmas have densities 10^{15}–10^{17} m^{-3}, electron temperatures $\leqslant 10$ eV, and plasma potentials $V_p = 10$–20 V.

In experiments dealing with fast ions [19,20], a simple magnetized torus (SMT) configuration [18] is used where a small vertical field $B_z \approx 2$ mT is superposed on a dominant toroidal field $B_\phi \approx 74$ mT (on axis). Magnetic field lines are therefore open and helical in shape, as shown in Fig. 10. In this particular configuration, plasma structures are elongated
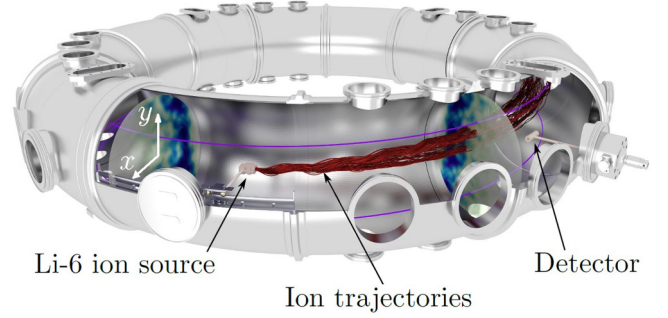

FIG. 10. Fast ion propagation in TORPEX. The toroidal vessel contains a hydrogen plasma in an SMT configuration with open helical magnetic field lines. A Li-6+ source injects fast lithium ions into the plasma. These ions then propagate towards a detector positioned at a different toroidal location. Interaction with the turbulent plasma potential (depicted at two toroidal locations, one near the source and the other near the detector) affects the ion trajectories and introduces variations in the number of ions that reach the detector. The detector can be moved in the x and y directions (indicated in white) to perform measurements at different locations on the same xy (poloidal) plane.

along the B-field lines [30–32] and, therefore, plasma parameters exhibit an approximately 2D spatial variation (perpendicular to the B field). Some field-aligned structures can detach intermittently [33] from the plasma and propagate radially outward [34] (in the direction of increasing x), giving rise to so-called *blobs* [35–37].

We use the Boris algorithm [38] to simulate the propagation of Li-6 ions in a volume with the prescribed SMT magnetic field and a time-varying electric field (Fig. 10) associated to the presence of the plasma. This E field, in fact, is just the gradient of the plasma potential V_p. We use, as a proxy for V_p, 2D-resolved floating potential measurements [39,40] rescaled such that the magnitude of the gradients agrees with E-field fluctuation profiles obtained with a triple probe [41]. The fast ions act as tracers and do not affect the fields.

Li-6 ions are generated in bunches of $N = 1.6 \times 10^5$ particles on the poloidal plane of the source. They initially have a 2D Gaussian density profile of widths $\text{w}_x = \text{w}_y = 1$ mm, centered at $(x, y) = (-1, -13.5)$ cm. The initial ion speed is random and distributed 1D *Normal* such that the kinetic energy is (30 ± 0.3) eV. As the average energy is much higher than typical ion temperatures (<1 eV), the Li-6 ions are suprathermal, or *fast*. The initial direction is almost parallel to the B field, with a 2D *Normal* distribution with width $4.3°$ and a mean angle of $5.6°$ above the toroidal direction (see Fig. 10).

The ion motion is integrated until ions reach the toroidal location of the detector, 171.3 cm apart. Ions can only be lost to the wall, since collisions with neutrals and plasma constituents are negligible [20]. Although ions may spread toroidally, due for example to the differences in initial conditions, we include all ions in the same bunch as contributing to the same detection signal. The detector is modeled as having efficiency 1 within a circle of radius 4 mm and zero outside. Thus any ions that arrive within the collection circle centered at $\mathbf{R} = (X, Y)$ are counted and generate one sample of number of detected particles, for example, $N_1(\mathbf{R})$. We model the
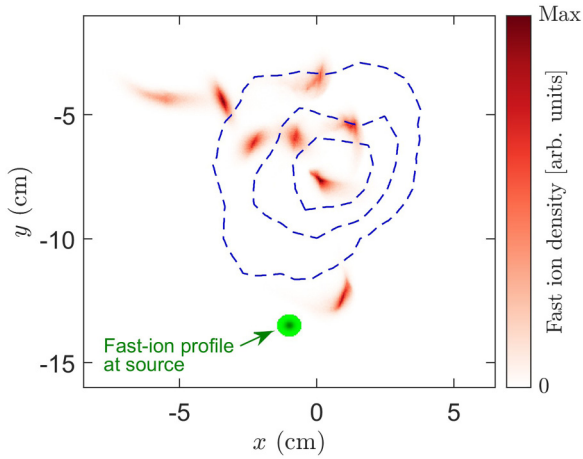
FIG. 11. Some fast ion bunches as they arrive at the xy (poloidal) plane of the detector. Different bunches (shaded structures) arrive at different locations after propagating through the turbulent plasma. Darker parts correspond to higher density of ions, as per the color bar. Comparison with the shape and location of the bunches as injected at the source (indicated in the figure) shows that fast ions experience drifts as well as shear. Once the effects of the detector are added, $\langle N(\mathbf{r}) \rangle$ can be computed. Contour lines of the result (blue dashed lines) show a time-averaged profile that is much wider than the individual bunches.

situation of a continuous ion *beam* by injecting bunches every 4 μs. Then, the TSN at detector location $\mathbf{R}$ will consist of the collection of detected samples for all $K = 1.1 \times 10^4$ bunches $\{N_k(\mathbf{R})\}$. Formally, this situation is different from Sec. IV as now many similar bunches arrive (one at a time) on a plane instead of having a single bunch that moves on the plane. However, the conditions are analogous in the two cases (see Fig. 11). Finally, by displacing the detector, we obtain a collection of TSNs as a function of location, in the xy plane, whose average $\langle N(\mathbf{r}) \rangle$ is the AP of Li-6 ions.

Since the floating potential profiles evolve in time, the arrival location of the Li-6 ions changes with time. Figure 11 shows simulation results of ions as they reach the poloidal plane of the detector. Interestingly, the ions are still bunched in xy and are small compared to the AP. They wander around in xy as illustrated in Fig. 9. They, however, are somewhat deformed, which can be understood by remembering that local variations of the turbulent plasma potential have a direct effect on fast ion displacement across magnetic field lines through $\mathbf{E} \times \mathbf{B}$ drifts [28,42]. In our simulations, the spatial variation $\Delta|\mathbf{E}|$ of the E field over a distance of 1 cm (in the order of the beam cross section; see Fig. 11) is typically < 17 V/m. This value is an average computed over the region in the xy plane in which the ion beam propagates, taking into account both the x and the y components of the E field. However, $\Delta|\mathbf{E}|$ can reach values as high as 250 V/m over 1 cm, which can lead to significant particle divergence even for short interaction times. For example, if two particles ≈ 1 cm apart within the same bunch are subject to this field gradient for 1 μs (the typical propagation time is 56 μs), their final separation will increase by ≈ 1 μs $\Delta|\mathbf{E}|/B_\phi = 3.4$ mm. In that case we expect significant changes in shape. This estimate does not include gyro averaging [19,20,42] from the
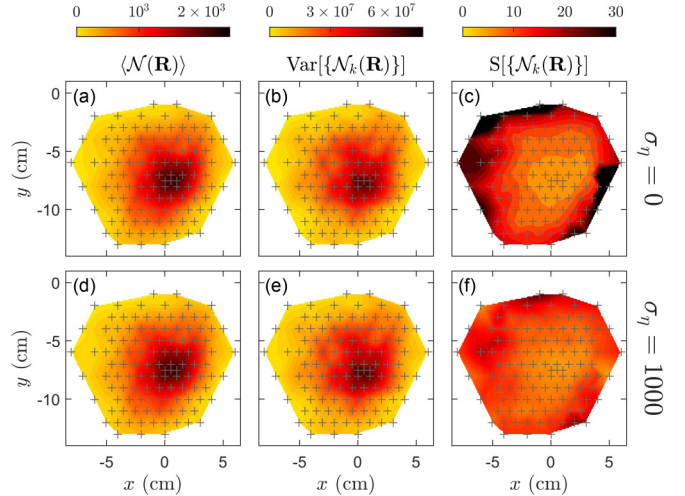

FIG. 12. Fast-ion simulation results. TSNs are determined for ≈ 100 choices of detector location ("+" markers) and the mean, variance, and skewness are computed. The results are then linearly interpolated between the markers and the outcome is plotted following the color map in each column. TSNs are dimensionless, as they hold data in units of *number of particles*. (a) Mean, (b) variance, and (c) skewness for the case of no noise. (d), (e), (f) Same statistics when Gaussian noise with *zero* mean and $\sigma_\eta = 10^3$ is added to all TSNs. Even though the mean and variance remain similar, a comparison of (c) and (f) confirms that low levels of noise can have a big impact on the skewness.

≈ 5 mm radius gyro orbits, nor drift averaging [19,20], whose effect is included in the simulations but is difficult to quantify in a simple way.

In Sec. V B we show that the theory of Sec. IV describes well the relationship between TSN statistics, despite the beam deformations and the slightly altered response efficiency function used for the detector.

B. Simulation results for 30 eV ions

Figure 12 shows the mean, variance, and skewness of simulated TSNs as a function of detector location. The plot of the mean is then the AP of the fast ions. To illustrate the impact of noise on the profiles of the different statistics, we make a comparison with the case of added Gaussian noise (*zero* skewness).

From Sec. V A, we know that $N = 1.6 \times 10^5$ and $A_{\mathrm{eff}} = \pi \, (4 \text{ mm})^2 = 50.2 \text{ mm}^2$. We use these numbers to normalize the variance and plot it against the normalized mean, similarly as in Fig. 5. The result [Fig. 13(a)] shows an approximately linear relationship, with a quadratic correction, as expected from Eq. (43). In fact, a least-squares fit of the data gives a value $n_A^{\max} = 7348 \text{ m}^{-2}$, which is in reasonable agreement with simulated bunch widths corrected to account for the finite detector width. Indeed, assuming a Gaussian-shaped bunch, the discussion following Eq. (41) allows us to estimate $\mathrm{w}_{nA} \approx 1/\sqrt{2\pi \, n_A^{\max}} = 4.7$ mm.

Figure 13(b) shows TSN skewness versus normalized mean. Using the value of $n_A^{\max}$ determined above, we plot the predicted skewness [Eq. (44)] and find good agreement with the simulations. Some discrepancies are observed, but they
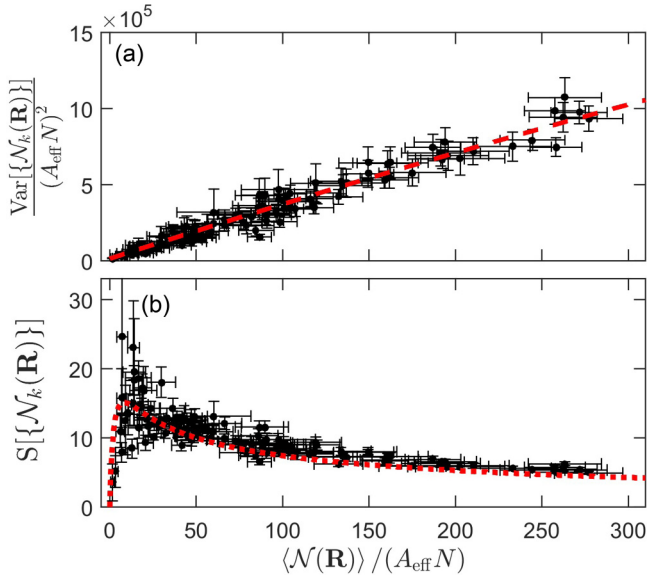
FIG. 13. Normalized variance (a) and skewness (b) of the simulated fast ion TSNs, plotted against the mean. Gaussian noise with *zero* mean and $\sigma_\eta = 10^3$ has been added to all TSNs. Each black dot corresponds to statistics computed for a single TSN from one particular detector location ("+" markers in Fig. 12). The error bars are 1σ uncertainties estimated using simple bootstrapping with nonoverlapping blocks of 500 samples from the corresponding TSN (changing the block size does not appreciably alter the outcome). The red dashed curve in (a) is a fit of the data using Eq. (43) as a model. The fit allows us to determine the parameter $n_A^{\max}$, which can then be replaced in Eq. (44) to produce a predicted skewness curve [red dotted line in (b)] for an assumed Gaussian-shaped bunch. There is good agreement between the model and the simulations.

are reasonably expected from the fact that fast ions exhibit behavior that is more complex than the simple assumptions used in the model of Sec. IV.

VI. CONCLUSIONS

We have developed a simple model to study the relationship between the average profile (AP) and higher-order statistics of time series of number of detected particles (TSNs) in systems where a detector counts particles of a moving density profile.

We started with the 1D case and showed that the PDF of the particle bunch center locations is closely related to the AP. This result was deemed fundamental, since the computation of the variance, skewness, kurtosis, and higher-order moments of TSNs, as well as the covariance, were shown to rely on the knowledge of this PDF.

Using all Gaussian shapes, we then obtained exact results in 1D. This allowed us to make a detailed comparison of theoretical predictions with statistics computed from numerically generated TSNs. The notable level of agreement between them showed that the theory gives a correct description of the problem.

An important observation is that many different values of skewness are possible in a single AP. Care must therefore be

taken when drawing conclusions from the skewness of distinct time series, as any difference may be related to differences in the detector location (within a single AP) and not necessarily to changes of APs. This consideration may be specially important in transport studies, where one is interested in determining changes of APs to establish, for example, diffusion properties [20] of the system.

The exact results also allowed us to benchmark a series of approximations carried out to extend the applicability of the formalism to the case of non-Gaussian APs. These approximations show that, under certain conditions, knowledge of the AP and a few other parameters is enough to determine the value of the variance, skewness, and covariances of the TSNs in *all* possible locations of the detector. The procedure can easily be extended for higher-order moments such as the kurtosis.

Bunch shapes different than Gaussian can easily be considered and lead to slight modifications of the expressions for the approximated statistics. Conversely, it was shown that single TSNs can be used to gain knowledge into the shape of the particle bunch, an observation that may be useful in situations where detectors cannot be displaced and there is interest in establishing spatial features of the instantaneous bunch profile.

Incorporation of noise was shown to have potentially significant effects on the TSN statistics, most notably on the value of the skewness. Indeed, problems seem to arise at locations visited only scarcely by the bunch (low values in the AP), as the detection signal variance tends to vanish and noise starts dominating. Since the variance enters in the calculation of the skewness through the denominator, even small values of noise may have a big impact. This observation motivates exploring the use of alternatives to the skewness which do not require normalization by the variance.

The theory was extended to 2D and applied to studies of fast ion propagation in TORPEX. The results show that the formalism is robust and may be used in realistic situations. Future experiments with fast ions are envisioned in TORPEX to further test these ideas.

We showed that simulations using a large number of samples K lead to results that are consistent with the theory developed in the paper. However, one outstanding question is how robust TSN statistics are for different sample sizes. Further dedicated numerical studies with larger K may be required.

The formalism can be straightforwardly used to model other systems. For example, one can replace N by I and $n(\mathbf{r})$ by $J(\mathbf{r})$ in studies dealing with samples of current and (moving) current density profiles.

APPENDIX: COMPUTATION OF m_q FOR 1D GAUSSIAN PROFILES

This Appendix refers to the discussion and results of Sec. II B.

In the case of 1D Gaussian profiles, $n_L(x) = \mathrm{G}(x; 0, \mathrm{w}_{nL}^2)$, we can express $[n_L(x)]^q$ as

$$
[n_L(x)]^q = \left(\frac{1}{\sqrt{2\pi\,\mathrm{w}_{nL}^2}} e^{-\frac{x^2}{2\mathrm{w}_{nL}^2}} \right)^q
$$

$$
= \frac{1}{\sqrt{q}} \left(\frac{1}{\sqrt{2\pi\,\mathrm{w}_{nL}^2}} \right)^{q-1} \mathrm{G}\left(x; 0, \mathrm{w}_{nL}^2/q\right). \quad \text{(A1)}
$$

Since $f(x) = \mathrm{G}(x; c_m, \sigma_f^2)$ with $\sigma_f = \sqrt{\mathrm{w}_m^2 - \mathrm{w}_{nL}^2}$ for the case when $m(X) = \mathrm{G}(X; c_m, \mathrm{w}_m^2)$, we have

$$
m_q(X) = \int [n_L(X-x)]^q f(x)\,dx
$$

$$
= \frac{1}{\sqrt{q}\,\left(2\pi\,\mathrm{w}_{nL}^2\right)^{\frac{q-1}{2}}} \int \mathrm{G}\left(X-x; 0, \mathrm{w}_{nL}^2/q\right)
$$

$$
\times\, \mathrm{G}\left(x; c_m, \sigma_f^2\right)dx
$$

$$
= \frac{1}{\sqrt{q}\,\left(2\pi\,\mathrm{w}_{nL}^2\right)^{\frac{q-1}{2}}} \mathrm{G}\left(X; c_m, \frac{\mathrm{w}_{nL}^2}{q} + \sigma_f^2\right). \quad \text{(A2)}
$$

The last line comes from the fact that the convolution of two normalized Gaussians is a normalized Gaussian. Notice that m_q need not be normalized, as it is preceded by a factor that is in general different from 1 for $q > 1$. The width of the Gaussian in the last line is

$$
\frac{\mathrm{w}_{nL}^2}{q} + \sigma_f^2 = \frac{\mathrm{w}_{nL}^2}{q} + \left(\mathrm{w}_m^2 - \mathrm{w}_{nL}^2\right)
$$

$$
= \mathrm{w}_m^2 \left(1 - \frac{\mathrm{w}_{nL}^2}{\mathrm{w}_m^2}\left(1 - \frac{1}{q}\right) \right)
$$

$$
= \mathrm{w}_m^2 s_q^{-1},
$$

where s_q is defined as in Eq. (15). Then, an argument similar to Eq. (A1) can be used to show that

$$
\mathrm{G}\left(x; c_m, \frac{\mathrm{w}_m^2}{s_q}\right) = \sqrt{s_q}\left(2\pi\,\mathrm{w}_m^2\right)^{\frac{s_q-1}{2}} \left(\mathrm{G}\left(x; c_m, \mathrm{w}_m^2\right)\right)^{s_q}
$$

$$
= \sqrt{s_q}\left(2\pi\,\mathrm{w}_m^2\right)^{\frac{s_q-1}{2}} (m(x))^{s_q}.
$$

Replacing this result back in Eq. (A2) we get

$$
m_q(X) = \frac{\sqrt{s_q}\left(2\pi\,\mathrm{w}_m^2\right)^{\frac{s_q-1}{2}}}{\sqrt{q}\,\left(2\pi\,\mathrm{w}_{nL}^2\right)^{\frac{q-1}{2}}} (m(X))^{s_q}.
$$

This expression is equivalent to Eq. (14).

[1] D. Perrone, R. O. Dendy, I. Furno, R. Sanchez, G. Zimbardo, A. Bovet, A. Fasoli, K. Gustafson, S. Perri, P. Ricci and F. Valentini, Nonclassical transport and particle-field coupling: from laboratory plasmas to the solar wind, Space Sci. Rev. **178**, 233 (2013).

[2] H. Tananbaum, M. C. Weisskopf, W. Tucker, B. Wilkes, and P. Edmonds, Highlights and discoveries from the Chandra X-ray Observatory, Rep. Prog. Phys. **77**, 066902 (2014).

[3] A. M. Keesee and E. E. Scime, Neutral argon density profile determination by comparison of spectroscopic measurements and a collisional-radiative model, Rev. Sci. Instrum. **77**, 10F304 (2006).

[4] V. V. Deshpande, S. Hsieh, A. W. Bushmaker, M. Bockrath, and S. B. Cronin, Spatially Resolved Temperature Measurements of Electrically Heated Carbon Nanotubes, Phys. Rev. Lett. **102**, 105501 (2009).

[5] S. D. Hogan and F. Merkt, Demonstration of Three-Dimensional Electrostatic Trapping of State-Selected Rydberg Atoms, Phys. Rev. Lett. **100**, 043001 (2008).

[6] J. Fraden, *Handbook of Modern Sensors*, 4th ed. (Springer, New York, 2010).

[7] P. A. Probst and B. Collet, Low-frequency digital lock-in amplifier, Rev. Sci. Instrum. **56**, 466 (1985)

[8] P. Wizinowich *et al.*, First light adaptive optics images from the Keck II telescope: A new era of high angular resolution imagery, Publ. Astron. Soc. Pac. **112**, 315 (2000).

[9] J. A. Dowling and P. M. Livingston, Behavior of focused beams in atmospheric turbulence: Measurements and comments on the theory, J. Opt. Soc. Am. **63**, 846 (1973).

[10] L. C. Andrews and R. L. Phillips, *Laser Beam Propagation Through Random Media*, 2nd ed. (SPIE Press, Bellingham, WA, 2005), pp. 201–206.

[11] O. Chellai, S. Alberti, M. Baquero-Ruiz, I. Furno, T. Goodman, F. Manke, G. Plyushchev, L. Guidi, A. Koehn, O. Maj, E. Poli, K. Hizanidis, L. Figini, and D. Ricci, Millimeter-Wave Beam Scattering by Field-Aligned Blobs in Simple Magnetized Toroidal Plasmas, Phys. Rev. Lett. **120**, 105001 (2018).

[12] A. Köhn, E. Holzhauer, J. Leddy, M. B. Thomas, and R. G. L. Vann, Influence of plasma turbulence on microwave propagation, Plasma Phys. Control. Fusion **58**, 105008 (2016).

[13] G. Janacek, *Practical Time Series* (Arnold, London, 2001).

[14] F. Militello, T. Farley, K. Mukhi, N. Walkden, and J. T. Omotani, A two-dimensional statistical framework connecting thermodynamic profiles with filaments in the scrape off layer and application to experiments, Phys. Plasmas **25**, 056112 (2018).

[15] F. Militello and J. T. Omotani, Scrape off layer profiles interpreted with filament dynamics, Nucl. Fusion **56**, 104004 (2016).

[16] G. I. Taylor, The spectrum of turbulence, Proc. R. Soc. A **164**, 476 (1938).

[17] S. Perri and A. Balogh, Stationarity in solar wind flows, Astrophys. J. **714**, 937 (2010).

[18] I. Furno, F. Avino, A. Bovet, A. Diallo, A. Fasoli, K. Gustafson, D. Iraji, B. Labit, J. Loizu, S. H. Müller, G. Plyushchev, M. Podesta, F. M. Poli, P. Ricci, and C. Theiler, Plasma turbulence, suprathermal ion dynamics and code validation on the basic plasma physics device TORPEX, J. Plasma Phys. **81**, 345810301 (2015).

[19] A. Bovet, Suprathermal ion transport in turbulent magnetized plasmas, Ph.D. dissertation, Ecole Polytechnique Fédérale de Lausanne, Switzerland, 2015.

[20] A. Bovet, A. Fasoli, P. Ricci, I. Furno, and K. Gustafson, Non-diffusive transport regimes for suprathermal ions in turbulent plasmas, Phys. Rev. E **91**, 041101 (2015).

[21] R. D. Yates and D. J. Goodman, *Probability and Stochastic Processes: A Friendly Introduction for Electrical and Computer Engineers*, 3rd ed. (John Wiley and Sons, Hoboken, NJ, 2014).

[22] W. B. Davenport and W. L. Root, *An Introduction to the Theory of Random Signals and Noise* (IEEE Press, New York, 1987).

[23] A. Gut, *An Intermediate Course in Probability*, 2nd ed. (Springer, New York, 2009).

[24] G. Schay, *Introduction to Probability with Statistical Applications* (Birkhauser, Boston, MA, 2007).

[25] D. N. Joanes and C. A. Gill, Comparing measures of sample skewness and kurtosis, J. R. Stat. Soc. (Ser. D) **47**, 183 (1998).

[26] See https://www.mathworks.com/products/matlab.html for a description of the MATLAB software, v. R2015a.

[27] G. Vasilescu, *Electronic Noise and Interfering Signals* (Springer, Berlin, 2005).

[28] P. M. Bellan, *Fundamentals of Plasma Physics* (Cambridge University Press, Cambridge, UK, 2006).

[29] M. Podesta, A. Fasoli, B. Labit, M. McGrath, S. H. Müller, and F. M. Poli, Plasma production by low-field side injection of electron cyclotron waves in a simple magnetized torus, Plasma Phys. Control. Fusion **47**, 1989 (2005).

[30] F. M. Poli, P. Ricci, A. Fasoli, and M. Podesta, Transition from drift to interchange instabilities in an open magnetic field line configuration, Phys. Plasmas **15**, 032104 (2008).

[31] P. Ricci, F. D. Halpern, S. Jolliet, J. Loizu, A. Mosetto, A. Fasoli, I. Furno, and C. Theiler, Simulation of plasma turbulence in scrape-off layer conditions: The GBS code, simulation results and code validation, Plasma Phys. Control. Fusion **54**, 124047 (2012).

[32] S. H. Müller, C. Theiler, A. Fasoli, I. Furno, B. Labit, G. R. Tynan, M. Xu, Z. Yan, and J. H. Yu, Studies of blob formation, propagation and transport mechanisms in basic experimental

plasmas (TORPEX and CSDX), Plasma Phys. Control. Fusion **51**, 055020 (2009).

[33] B. Labit, A. Diallo, A. Fasoli, I. Furno, D. Iraji, S. H. Müller, G. Plyushchev, M. Podesta, F. M. Poli, and P. Ricci, Statistical properties of electrostatic turbulence in toroidal magnetized plasmas, Plasma Phys. Control. Fusion **49**, B281 (2007).

[34] C. Theiler, I. Furno, A. Fasoli, P. Ricci, B. Labit, and D. Iraji, Blob motion and control in simple magnetized plasmas, Phys. Plasmas **18**, 055901 (2011).

[35] I. Furno, B. Labit, M. Podesta, A. Fasoli, S. H. Müller, F. M. Poli, P. Ricci, C. Theiler, S. Brunner, A. Diallo, and J. Graves, Experimental Observation of the Blob-Generation Mechanism from Interchange Waves in a Plasma, Phys. Rev. Lett. **100**, 055004 (2008).

[36] I. Furno, M. Spolaore, C. Theiler, N. Vianello, R. Cavazzana, and A. Fasoli, Direct Two-Dimensional Measurements of the Field-Aligned Current Associated with Plasma Blobs, Phys. Rev. Lett. **106**, 245001 (2011).

[37] I. Furno, C. Theiler, D. Lançon, A. Fasoli, D. Iraji, P. Ricci, M. Spolaore, and N. Vianello, Blob current structures in TORPEX plasmas: Experimental measurements and numerical simulations, Plasma Phys. Control. Fusion **53**, 124016 (2011).

[38] H. Qin, S. Zhang, J. Xiao, J. Liu, Y. Sun, and W. M. Tang, Why is Boris algorithm so good?, Phys. Plasmas **20**, 084503 (2013).

[39] M. Baquero-Ruiz, F. Avino, O. Chellai, A. Fasoli, I. Furno, R. Jacquier, F. Manke, and S. Patrick, Dual Langmuir-probe array for 3D plasma studies in TORPEX, Rev. Sci. Instrum. **87**, 113504 (2016).

[40] S. H. Müller, A. Diallo, A. Fasoli, I. Furno, B. Labit, G. Plyushchev, M. Podesta, and F. M. Poli, Probabilistic analysis of turbulent structures from two-dimensional plasma imaging, Phys. Plasmas **13**, 100701 (2006).

[41] C. Theiler, I. Furno, A. Kuenlin, Ph. Marmillod, and A. Fasoli, Practical solutions for reliable triple probe measurements in magnetized plasmas, Rev. Sci. Instrum. **82**, 013504 (2011).

[42] K. Gustafson, P. Ricci, I. Furno, and A. Fasoli, Nondiffusive Suprathermal Ion Transport in Simple Magnetized Toroidal Plasmas, Phys. Rev. Lett. **108**, 035006 (2012).